Ciprofloxacin Removal via Acid-Modified Red Mud: Optimizing the Process, Analyzing the Adsorption Features, and Exploring the Underlying Mechanism

Jingzhuan Shi *, Wanqiong Wang , Ziyi Li , Yingjuan Shi

Posted Date: 23 May 2024

doi: 10.20944/preprints202405.1520.v1

Keywords: acidified red mud; ciprofloxacin; adsorption; response surface methodology

Article

Ciprofloxacin Removal via Acid-Modified Red Mud: Optimizing the Process, Analyzing the Adsorption Features, and Exploring the Underlying Mechanism

Jingzhuan Shi [1,*], Wanqiong Wang [1], Ziyi Li [1] and Yingjuan Shi [2]

[1] School of Chemistry and Environmental Science, Shaanxi University of Technology, Han Zhong 723001, China

[2] Shaanxi Reconnaissance Design & Research Institute of Water Environmental Engineering, Xi'an 710021, China

Abstract: RM (red mud) was acidified with sulphuric acid and the acidified ARM (acidified red mud) was utilized as an innovative adsorption material for treating antibiotic-contained wastewater. The adsorption conditions, kinetics, isotherms, thermodynamics, and mechanism of ARM for CIP (ciprofloxacin) were investigated. Characterization of the ARM involved techniques such as scanning electron microscopy(SEM), transmission electron microscope(TEM), brunauer-emmett-teller (BET), X-ray diffraction (XRD), X-ray fluorescence (XRF), thermogravimetric analysis (TGA) and NH_3-TPD analysis. Adsorption studies were conducted employing response surface methodology (RSM) for experimental design. The results showed that ARM can absorb CIP effectively. The RSM optimal experiment indicated that the most significant model terms influencing adsorption capacity were solution pH, CIP initial concentration and ARM dosage, under which the predicted maximum adsorption capacity achieved 7.30 mg/g. The adsorption kinetics adhered to a pseudo-second-order model, while equilibrium data fitted the Langmuir-Freundlich isotherm, yielding maximum capacity values of 7.35 mg/g. The adsorption process occurred non-spontaneously and absorbed heat, evidenced by ΔG^0 values between 2.06 and 0.87 kJ/mol, ΔS^0 at 39.41 J/mol/K, and ΔH^0 at 13.8 kJ/mol. Analysis using attenuated total reflection Fourier-transform infrared spectroscopy (ATR-FTIR) indicated there existed complex reaction between Al-O in ARM and the ester group –COO in CIP. The C=O bond in CIP was likely to undergo a slight electrostatic interaction or be bound to the internal spherical surface of ARM. The findings indicate that ARM is a promising and efficient adsorbent for CIP removal from wastewater.

Keywords: acidified red mud; ciprofloxacin; adsorption; response surface methodology

1. Introduction

Red mud (RM) is a by-product generated from bauxite ore processing with caustic soda during alumina manufacturing. (Jollet, Gissane and Schlaf, 2014; Wu J., et al., 2018). It was estimated that RM amount reached 3.5×10^9 tons in 2014 worldwide (Ren et al., 2019). In China, the annual yield of RM is 7×10^7 tons and the accumulated inventory is about 6×10^8 tons (Xue et al., 2016). Thus, the large amount of RM has posed serious environmental problems. Currently, the primary method for RM disposal involves using it for dam construction, while the secondary contamination induced by RM's high alkalinity occurs frequently (Schmalenberger et al., 2013; Ren et al., 2018). Therefore, RM utilization has increasingly received the public concern (Hua, Heal and Friesl, 2017). So far, various attempts have been made to exploit RM, including the production of building materials, the recycling of rare metals, the preparation of RM-based catalysts and adsorbents, etc (Gu, Wang and Liu, 2012; Zhu et al., 2017; Yan et al., 2018; Wang et al., 2016). Nevertheless, the adsorption performance of RM was mainly focused on the removal of heavy metal ions, organic dyes and phosphorus, etc (Li et al.,

 doi:10.20944/preprints202405.1520.v1

2018; Wang et al., 2015; Ye et al., 2015). To the best of our understanding, there has been limited research on RM's capacity to adsorb antibiotic contaminants.

Fluoroquinolone antibacterial agents (FQs), a class of powerful synthetic antibiotics, are extensively utilized in both human and veterinary healthcare(Walsh, 2003). Their pervasive use raises concerns as FQs can infiltrate aquatic ecosystems through various pathways, including effluents from pharmaceutical manufacturing, sewage sludge, and agricultural waste. Investigations have increasingly found FQs present in various water bodies. Notably, studies in the U.S. identified four FQs—ciprofloxacin, norfloxacin, enrofloxacin, and sarafloxacin—with average concentrations ranging up to 0.12 μg/L in surface waters(Kolpin, Furlong and Meyer, 2002). Furthermore, ciprofloxacin has been found in hospital wastewater at concentrations between 19-155 μg/L, indicating a significant potential for environmental contamination(Martins, et al., 2008). Even at low levels, the presence of these antibiotics in water poses a risk to both ecosystems and human health, with some contributing to bacterial genotoxicity in sewage(Orimolade, et al., 2023). To mitigate this risk, methods such as ozonation, photocatalysis, Fenton oxidation, and adsorption have been explored for FQ removal from water, with adsorption being particularly favored for its efficiency, ease of implementation, and cost-effectiveness(Ni et al., 2015).

In this research, we treated RM with sulfuric acid to create an adsorbent for extracting CIP from water. The altered RM, now termed ARM, underwent analysis to determine its morphology, structure, and characteristics using methods such as XRD, BET-BJH, SEM, TEM, XRF, TG-DSC, ATR-FTIR, and NH_3-TPD. We employed RSM utilizing a Box–Behnken design to fine-tune the adsorption parameters, including temperature, pH, initial CIP concentration, and ARM amount. This study also explored the adsorption kinetics, equilibrium isotherms, and thermodynamics associated with CIP removal by ARM. Furthermore, we delved into the underlying mechanisms of the CIP adsorption process on ARM.

2. Material and Methods

2.1. Materials

RM was taken from Shanxi Aluminum Corporation in Yuncheng City, Shanxi Province, China; pH value of the leaching solution was 11.04. CIP, possessing a purity exceeding 98%, was acquired from Tokyo Kasei Kogyo Co., Ltd. (TCI, Japan), with a molecular structure of $C_{17}H_{18}FN_3O_3$. The remainder of the chemicals used were of analytical quality, and all solutions were formulated using Millipore's ultra-pure water.

2.2. Methods

2.2.1. Preparation of ARM

Before acid treatment, RM underwent drying and was then finely milled to a size that would allow it to sieve through a 150-mesh (0.100 mm) screen. Then 50 g pre-treated RM was weighed and placed into a 1.0 L beaker, into which water was added under stirring until a liquid suspension was formed. The liquid-solid ratio of H_2SO_4 and RM was 0.5mL/g, the pH of the suspension was adjusted with H_2SO_4, and the pH of the suspension was 3.4 after stirring at 100r/min for 12h. After standing, the supernatant of mixture was rinced with water repeatedly until the supernatants pH became neutral. Finally, the solid residues were collected through vacuum filtration, dried at 100°C and sieved through 150-mesh screen for use.

2.2.2. Measurement of Adsorption Capacity

A certain amount of ARM (0.6, 0.8, 1.0 g) was added into 250-mL brown conical flask which contained 200 mL of a known concentration of CIP. The initial CIP concentrations tested were 10, 20, and 30 mg/L. The pH of the mixture was set to targeted levels (3.0, 5.0, 7.0, 9.0, 11.0±0.2) using 0.1 mol/L NaOH or HCl.Afterwards, the flask was sealed, shaken (HZ-8811K bath thermostat oscillator, Deou Corporation, Changzhou, China) at 250 rpm under the predetermined temperature (25, 35 or 45±1°C) for 180 min. Following centrifugation to isolate ARM, the clear supernatant was passed

 doi:10.20944/preprints202405.1520.v1

through a 0.22-μm membrane, preparing it for analysis via high-performance liquid chromatography (HPLC, Agilent 1200, USA). The blank control test (without addition of ARM) and three groups of parallel experiments were set up, and the results were documented as an average. The adsorption capacity was calculated by Equation (1):

$$q_t = \frac{(c_0 - c_t) \times v}{m} \quad (1)$$

Where:

q_t - the adsorption capacity (mg/g);
c_0 - CIP concentration at initial (mg/L);
c_t - CIP concentration at time t (mg/L);
v - solution volume (mL);
m - the mass of ARM (g).

2.2.3. Response Surface Optimization

After a series of single factor experiments, adsorption temperature, solution pH, CIP initial concentration, and ARM dosage were chosen as independent variables, which were recorded as A, B, C, and D, respectively. The choice of experimental conditions for each variable was informed by initial experimental outcomes. Table 1 displays the range of independent variables and their respective levels. The adsorption efficiency was designated as the response variable, Y.The optimization test scheme was designed by Box–Behnken RSM in Design Expert 10.7 software. The design matrix is given in Table 2.

Table 1. Variables and their respective ranges for the Box–Behnken experimental design.

Control factors	*Unit*	*Symbol*	*Real values and coded levels*		
			Low (-1)	*Mid (0)*	*High (1)*
Adsorption temperature	°C	A	25	35	45
Solution pH		B	3	7	11
CIP initial concentration	mg/L	C	10	20	30
ARM dosage	g/L	D	3	4	5

Table 2. Box–Behnken experimental design matrix.

Number	*A(°C)*	*B*	*C(mg/L)*	*D(g/L)*	*Number*	*A(°C)*	*B*	*C(mg/L)*	*D(g/L)*
1	25	11	20	4	**16**	25	7	20	3
2	35	7	30	3	**17**	25	7	10	4
3	25	3	20	4	**18**	35	3	20	5
4	35	7	10	5	**19**	35	7	30	5
5	35	7	20	4	**20**	45	11	20	4
6	45	7	20	5	**21**	35	7	10	3
7	35	3	10	4	**22**	25	7	30	4
8	25	7	20	5	**23**	35	7	20	4
9	35	11	30	4	**24**	35	7	20	4
10	35	3	30	4	**25**	35	11	20	5
11	45	7	20	3	**26**	35	7	20	4
12	45	7	30	4	**27**	35	7	20	4
13	45	7	10	4	**28**	35	11	10	4
14	35	11	20	3	**29**	45	3	20	4
15	35	3	20	3					

 doi:10.20944/preprints202405.1520.v1

2.2.4. Adsorption Kinetics

0.68 g of ARM and 200 mL CIP solution at 30 mg/L concentration were combined in a 250-mL brown conical flask. Solution pH was adjusted to 3.04. Then the flask was shaken at 250 rpm under25~55 °C. After an interval, a certain amount of mixed liquor was withdrawn for CIP analysis.

2.2.5. Adsorption Isotherm

This procedure mirrored the one outlined in Section 2.2.2, with equilibrium adsorption isotherms derived by altering CIP concentrations between 10 and 500 mg/L (pH =3.0±0.2) for a fixed amount of ARM (3.4 g/L) at temperatures(45 °C).

2.2.6. Analytical Methods

CIP levels were determined using HPLC (Agilent 1200 Series, Agilent, USA), employing a reversed phase XDB-C_{18} column (4.6 mm × 150 mm, 5 μm). The column was maintained at 30°C, with a 10 μL sample injection volume. The eluent consisted of acetonitrile and 0.2% formic acid in a 20:80 volume ratio. The flow rate was maintained at 0.2 mL/min, and UV detection was performed at 277 nm. Under which, the CIP retention time (t_R) was 9.768 min.

The texture, surface area, and pore size, composition of samples were analyzed by SEM (JSM-6700F,JEOL), TEM(JEM-3010, Japan),Barrett–Joyner–Halenda (BJH) and BET (V-Sorb 2800TP), XRD (XRD-7000, Shimadzu, Japan) and XRF (PANalytical Axios, Netherlands). The adsorption performance of samples were analyzed by TG (TGA/DSC^{3+}, Mettler Toledo) and NH_3-TPD(Bruker EMXplus,Germany).

The interaction of ARM and CIP at molecular scale was investigated using ATR-FTIR analysis. The samples were recorded on a VERTEX70 instrument (Bruker, Germany).

3. Results and Discussion

3.1. Adsorption Property of RM and ARM

According to Figure 1, under the same conditions, the adsorption capacity of CIP by RM after sulfuric acid acidification increased from 3.62 mg/g to 4.84 mg/g, and the removal rate increased from 61.41% to 82.21%. This indicates that ARM has significantly better adsorption performance for CIP than RM.

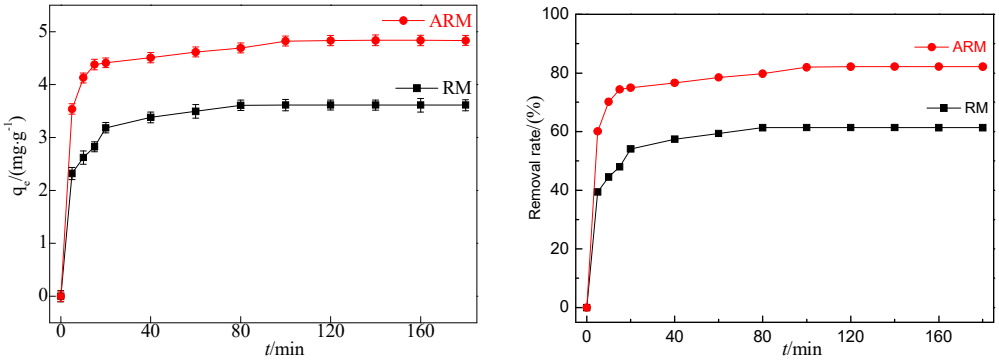

Figure 1. Effect of adsorption by RM and ARM (pH_0=3.04, T=45°C,[CIP]=20 mg/L,[RM]=3.4 g/L, [ARM]=3.4 g/L, r=250 rpm).

3.2. Characteristics of RM and ARM

3.2.1. Morphology of RM and ARM by SEM and TEM

SEM was utilized to assess the surface and structural characteristics of RM samples. Figure 2a shows that RM consists of spherical or flaky particles of micron size. Variations in particle size may result from the presence of both unchanged and newly formed minerals within the bauxite ore. The

 doi:10.20944/preprints202405.1520.v1

larger particles could either be the original minerals in the bauxite or aged mineral oxides (Atasoy, 2005). It is evident shown in Figure 2b that, ARM particles exhibit a broad spectrum of sizes and possess irregular shapes. These changes in size and morphology might be due to the dissolution of some minerals throughout the acidification process (Huang et al., 2008).

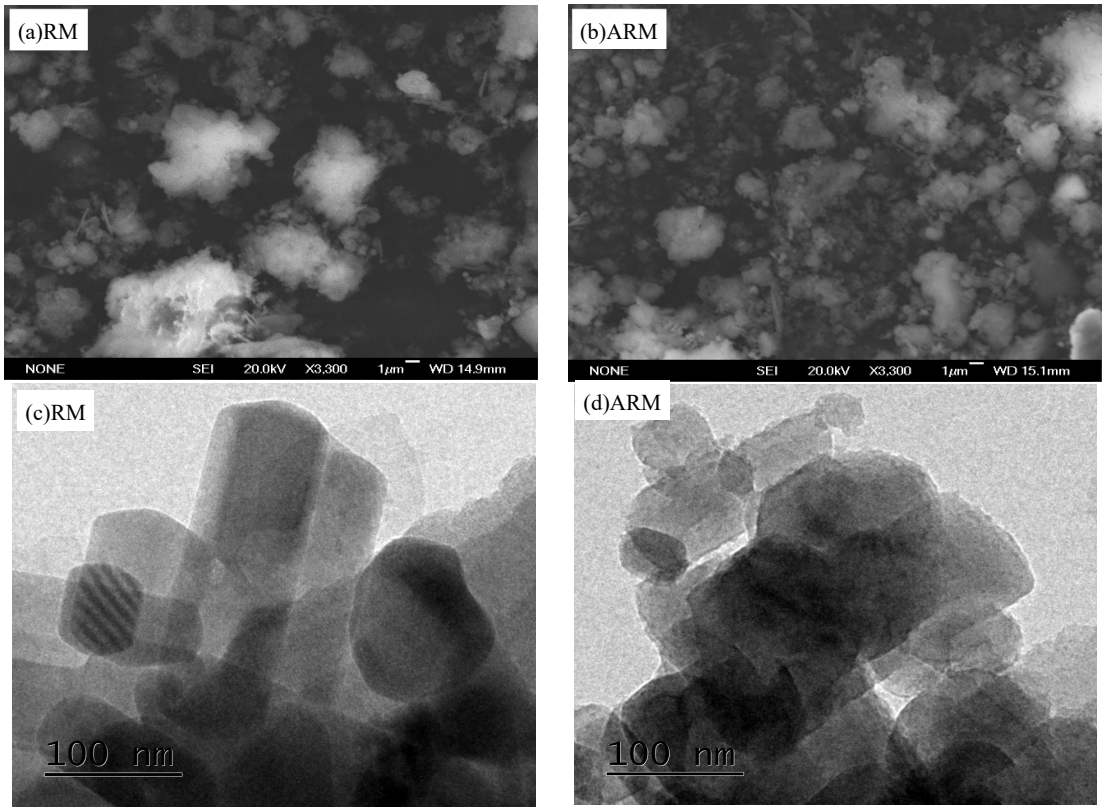

Figure 2. SEM images of RM (a) and ARM (b) and TEM images of RM (c) and ARM (d).

TEM analysis results showed that the round aggregates of RM (Figure 2c) were composed of fine particles and scattered irregular quadrilateral crystals, and were mainly porous frames with cemented connections, without definite shape(Jayasankar, et al.,2012). These may be some crystallized mineral phases and newly formed mineral phases in bauxite, which may be calcite, sodalite, silicates and iron oxides(manoj, et al.,2013). Figure 2d shows that RM is acidified, the internal crystal structure changes, and the crystal surface is corroded by acid.

3.2.2. BET–BJH Analysis

Figure 3 displays the nitrogen adsorption and desorption curves for both RM and ARM. both belong to type III(The curve has no inflection point and is convex downward throughout the pressure range). The surface areas of RM and ARM as measured by BET were calculated to be 10.96 and 17.44 m^2/g, respectively. ARM presented larger specific surface area and thus is more ready to adsorb CIP.

 doi:10.20944/preprints202405.1520.v1

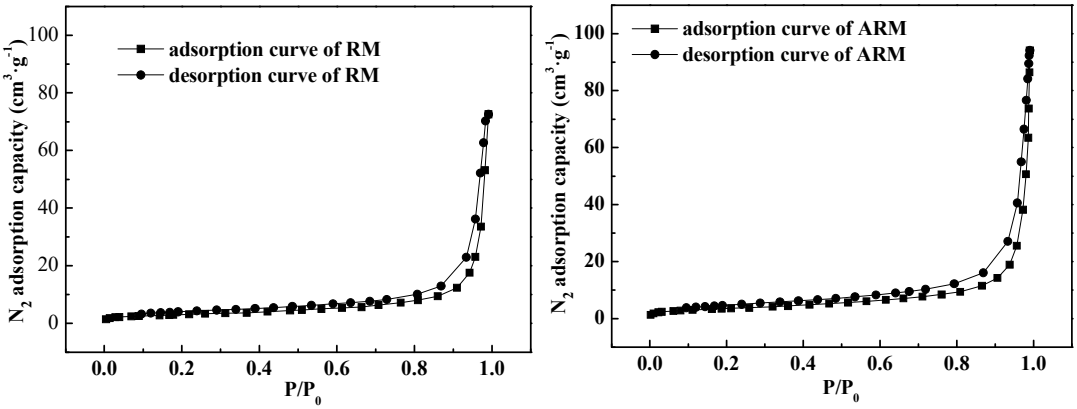

Figure 3. The N_2 adsorption/desorption isotherms for RM and ARM.

Figure 4 illustrates the pore size distributions for both RM and ARM. RM contains a small number of micropores and simple open porous channels. By contrast, the ARM contains not only micropores but also larger mesopores and macropores (micropores < 2.0 nm; smaller mesopores 2.0 -10.0 nm; larger mesopores and macropores ≥10 nm) (Zhilkina et al., 2013), the channel structure was very complex, with a peak appearing at 150 nm. The average pore size of RM and ARM were 40.93 and 45.41 nm, respectively. Which indicated that, acidification treatment contributed to the dissolution of aluminum, sodium, and/or silica compounds within RM, the primary surface structure of RM changed, so the porous channel widths increased.

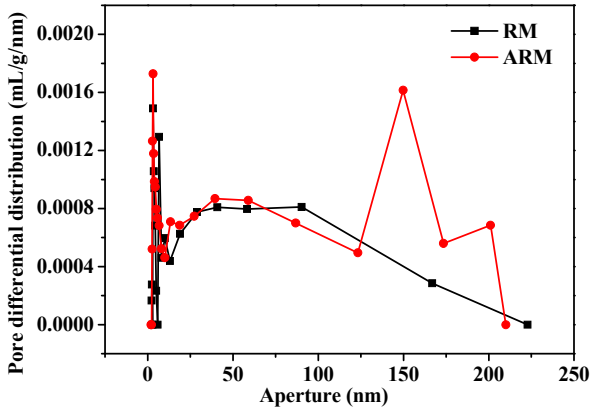

Figure 4. Pore size distribution of RM and ARM.

3.2.3. XRD and XRF Analysis

As depicted in Figure 5, XRD analysis revealed that the predominant component of the RM samples is Sodalite (S) ($Na_6(Al_6Si_6O_{24})CO_3$), Hematite(H)(Fe_2O_3), Gibbsite(G) ($Al(OH)_3$), Boehmite(B) (γ-AlO(OH)), TiO_2 (anatase and rutile), and quartz (SiO_2). The broad peaks observed in the XRD pattern are consistent with the findings reported by Guru et al. (Guru et al., 2019).

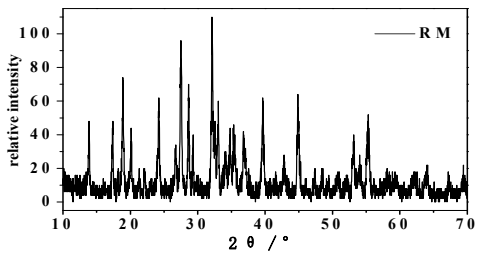

 doi:10.20944/preprints202405.1520.v1

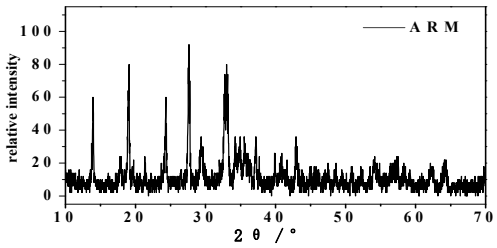

Figure 5. XRD patterns of RM(a) and ARM(b).

The XRF analysis results were showned in Table 3, indicating that after acidification treatment of RM, the CaO content rised from the original 26.01% to 40.13%. Iron oxide was a frequently encountered active constituent in catalysts(Fang, et al.,2023), Fe_2O_3 content rised from 11.56% to 28.37%.This phenomenon may be due to the fact that the crystals in the RM dissolve under the action of the acid, producing more iron oxide.The reduction in calcite phase within ARM is attributed to dissolution, leading to the generation of a more reactive surface conducive to CIP adsorption onto ARM (Deihimi, Irannajad and Rezai, 2018). Concurrently, the presence of Al_2O_3, SiO_2, and TiO_2 after modification could be attributed to their role as carriers(Liang, et al.,2024).

Table 3. The chemical compositions of both RM and ARM.

samples (%)	CaO	Al_2O_3	SiO_2	Na_2O	Fe_2O_3	TiO_2	K_2O	MgO	others
RM	26.01	23.72	17.09	11.76	11.56	5.72	1.81	0.95	1.38
ARM	40.13	8.36	10.89	2.10	28.37	4.26	2.91	1.13	1.85

3.2.4. TG-DSC Analysis

As depicted in Figure 6a,the total weight loss of RM from 24°C to 1100°C was 13.73%. Among them, the loss of 3% in the first stage from room temperature to 300°C was mainly due to the mass loss of red mud adsorbed water and internal structure water volatilization and partial hydroxide decomposition. For example, $Al(OH)_3$ was decomposed into AlO(OH), part of AlO(OH) was further decomposed into $Al_2O_3$and part of FeOOHwas decomposed into Fe_2O_3(Zhang, et al.,2010); In the second stage, the weight loss from 300°C to 600°C was 6.6%, mainly due to the mass loss of further decomposition of hydroxide. In the third stage, the weight loss from 600°C to 1100°C was 4.1%, which was mainly due to the mass loss of CO_2 released by thermal decomposition of calcium nepheline in red mud.

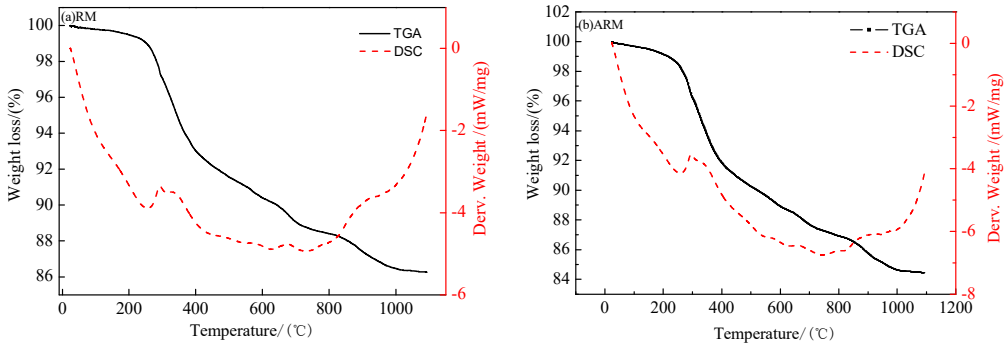

Figure 6. TGA-DSC of RM(a) and ARM(b).

As depicted in Figure 6b, the total weight loss of AaRM from 24°C to 1100°C was 15.55%. In the first stage, the weight loss from room temperature to 300°C was 3.8%, which was mainly due to the adsorption water of red mud and the evaporation of internal structural water. The weight loss of 7.3% and 4.4% in the second stage at 300°C~600°C and the third stage at 600°C~1100°C, respectively,

 doi:10.20944/preprints202405.1520.v1

was due to the loss of gas released by the thermal decomposition of hydrated garnet and calcium nepheline in the red mud.

The results of the TG analysis were compared with literature data (Liu, et al.,2007) in Table 4.

Table 4. Comparison study of TG analysis of ARM and RM sample.

Sample	Mass loss(%)	Temperature(°C)	References
Red mud (Zhengzhou Changcheng)	3	20~150	(Liu, et al.,2007)
	3.6	105~450	
	4.3	560~720	
Total	10.9	20~880	
Red mud (Shanxi Yuncheng)	3	25~300	In this present study
	6.6	300~600	
	4.1	600~1100	
Total	13.73	24~1100	
Acidified red mud (Shanxi Yuncheng)	3.8	25~300	In this present study
	7.3	300~600	
	4.4	600~1100	
Total	15.55	24~1100	

3.2.5. NH_3-TPD Analysis

The experimental results of NH_3-TPD are shown in Figure 7. As we all know, the adsorption capacity of the adsorbent is related to the number of active sites, the oxidation state of the active phase, the mobility of oxygen in the adsorbent matrix and other factors (Liang, et al.,2021).Peaks in the low temperature range of 100~300°C indicate that the physical adsorption of molecular oxygen and chemisorbed oxygen are desorbed above or near the surface of the adsorbent, peaks in the 300~500°Care attributed to the surface lattice oxygen in the adsorbent, and peaks in the high temperature range of 500~800°C are attributed to the bulk lattice oxygen of the adsorbent. The peak intensity of RM at about 245°C is extremely high, which is mainly the signal value generated by the decomposition of $CaCO_3$ in red mud into CO_2 at this temperature. In addition, RM has two small peaks at 495°C and 650°C, corresponding to desorption of surface oxygen vacancies and bulk oxygen vacancies. The peak of ARM appears at 500°C and 668°C respectively, compared with RM, which shifted towards high temperature, the peak strength increased, indicating that the interaction between sulfuric acid and Fe changed the electronic structure of the oxygen vacancy of the adsorbent, resulting in surface defects, providing a suitable adsorption site for oxygen molecules, and strengthening the adsorption capacity of oxygen species on the adsorbent.

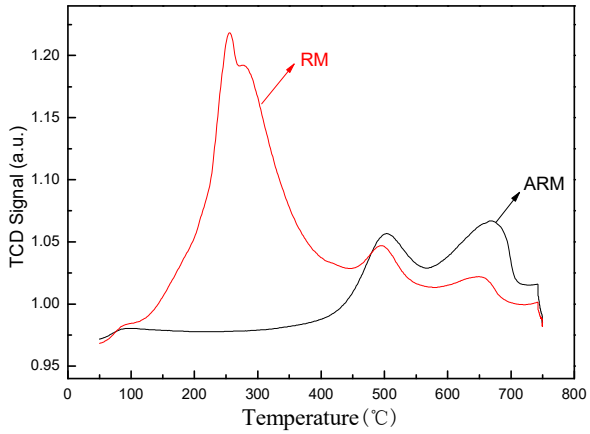

Figure 7. NH_3-TPD of RM(a) and ARM(b).

 doi:10.20944/preprints202405.1520.v1

3.3. Optimisation of Process Variables Using RSM

3.3.1. Establishment of the Model

According to the Box–Behnken method, response surface optimization for the adsorption conditions of CIP on RSM was made. The experimental design results are shown in Table 5.

Table 5. Box-Behnken design real values along with observed responses for CIP adsorption capacity.

Number	*Adsorption capacity (mg/g)*		*Number*	*Adsorption capacity (mg/g)*	
	Actual value	*Predicted value*		*Actual value*	*Predicted value*
1	2.35	2.34	**16**	2.99	3.08
2	4.07	4.47	**17**	1.28	1.02
3	4.78	4.90	**18**	3.82	4.08
4	1.04	0.72	**19**	2.76	2.89
5	2.34	2.34	**20**	2.18	2.24
6	1.94	1.74	**21**	1.66	1.62
7	2.28	2.77	**22**	3.21	3.53
8	2.34	2.09	**23**	2.34	2.34
9	3.32	2.72	**24**	2.34	2.34
10	7.23	6.70	**25**	1.85	2.22
11	3.11	3.24	**26**	2.34	2.34
12	3.16	3.44	**27**	2.34	2.34
13	1.22	0.93	**28**	1.21	1.63
14	2.99	2.76	**29**	4.78	4.80
15	6.37	6.02			

Under the different adsorption conditions designed in the test, the measured adsorption capacity of CIP varied from 1.04 to 7.23 mg/g. The results in Table 6 were further subjected to multiple regressions and variance analysis by employing Design Expert 10.7. The results, along with the corresponding data, are summarized in Table 5. Equation (2) presents a quadratic polynomial model representing adsorption capacity, incorporating four independent variables.

Table 6. ANOVA for the quadratic equation of the response surface.

Source	*Sum of squares*	*df*	*Mean square*	*F-value*	*P-value*
Model	56.73	11	5.16	40.08	< 0.0001
A	0.026	1	0.026	0.20	0.6595
B	19.66	1	19.66	152.77	< 0.0001
C	18.90	1	18.90	146.88	< 0.0001
D	4.61	1	4.61	35.83	< 0.0001
AD	0.067	1	0.067	0.52	0.4814
BC	2.01	1	2.01	15.66	0.0010
BD	0.50	1	0.50	3.89	0.0651
CD	0.11	1	0.11	0.88	0.3606
B^2	10.18	1	10.18	79.12	< 0.0001
C^2	0.084	1	0.084	0.65	0.4315
D^2	0.27	1	0.27	2.09	0.1662
Residual	2.19	17	0.13		
Lack of Fit	2.19	13	0.17		
Pure Error	0.000	4	0.000		
Cor Total	58.92	28			

 doi:10.20944/preprints202405.1520.v1

$$Y = 2.34 - 0.046A - 1.28B + 1.25C - 0.62D - 0.13AD - 0.71BC + 0.35BD$$
$$-0.17CD + 1.23B^2 - 0.11C^2 - 0.20D^2 \quad (2)$$

Where:

Y - the response variable (adsorption capacity) and the actual values of the predictors;

A - reaction temperature (°C);

B - solution pH;

C - CIP initial concentration (mg/L);

D - ARM dosage (g/L).

As shown in Table 6, *P* values of the parameters (involving B, C, D, BC, and B^2) were all lower than 0.05. Which implied that solution pH, CIP initial concentration, ARM dosage, interaction between pH and CIP initial concentration, and the effect of squares of pH all showed significant influences on the adsorption capacity. The *P* values of other parameters are larger than 0.05, indicating that other factors' effect on adsorption capacity is insignificant. Moreover, the high *F* value (F_{model}=40.08), and the associated very low probability value ($P < 0.0001$) of the model suggests statistical significance, indicating a well-fitted model.

Figure 8 shows the adsorption capacities between the calculated from the established quadratic polynomials and the measured ones. It was obvious that both the predicted and the measured values conform to a normal distribution, with a coefficient of determination $R^2 = 0.9629$, indicating that 96.3 % of all variation can be explained. Furthermore, the adjusted coefficient of determination (R^2_{Adj}) for the model stood at 0.9389, indicating a strong fit.The signal-to-noise ratio (SNR) is 25.92, much higher than 4, so the model is highly reliable, the data are reasonable. Therefore, Equation (2) can reflect the relationship between adsorption capacity and the variables accurately and reasonably.

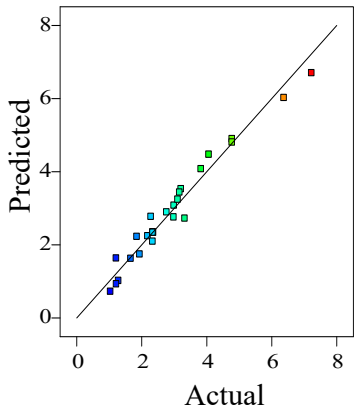

Figure 8. Comparison of the predicted and actual adsorption capacity (pH_0=3.04, T=45°C, [CIP]=30 mg/L, [ARM]=3.4 g/L,r=250 rpm).

3.3.2. Response Surface Analysis

Graphical representations of the models aid in comprehending the impacts of experimental variables on the responses. As mentioned, the interaction between solution pH and CIP initial concentration was significant. Figure 9 displays both the 3D surface graph and the corresponding contour plot illustrating the relationship between pH and CIP initial concentration. It is evident that adsorption capacity rises with increasing CIP initial concentration but decreases as solution pH decreases. Which was attributed to different dissociation forms of CIP at different pH. The CIP is mainly dissociated as H_4CIP^{3+} at low pH value. The chemical activity of H_4CIP^{3+} was stronger than H_3CIP^{2+}, more favorably adsorbed by the active materials in ARM (Saha and Sarkar, 2012). When the solution is alkaline, the active components in ARM are more readily precipitated, thus reducing the adsorption ability of ARM for CIP.

 doi:10.20944/preprints202405.1520.v1

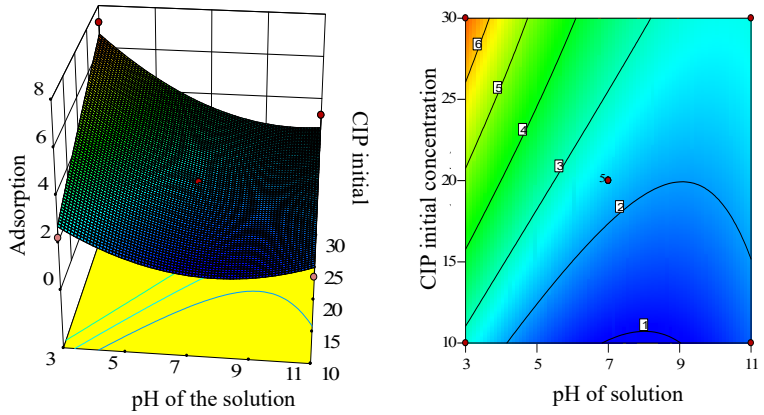

Figure 9. 3D surface graph and contour plot of solution pH and CIP initial concentration, 35°C and 3.0 g/L ARM.

3.3.3. Optimization Analysis

Numerical optimization was employed to determine the optimal conditions for CIP adsorption. Based on the fitted model, the optimal adsorption parameters were identified: temperature of 45°C, pH of 3.04, initial CIP concentration of 29.20 mg/L, ARM dosage of 3.40 g/L, resulting in an adsorption capacity of 7.30 mg/g.

3.4. Adsorption Kinetics

We utilized the pseudo-first-order and second-order kinetics, represented by Equations (3) and (4), to elucidate the sorption mechanism of CIP on ARM. Additionally, we employed the intraparticle diffusion model, Equation (5), to elucidate the diffusion mechanism.

$$\ln(q_e - q_t) = \ln(q_e) - k_1 t \quad (3)$$

$$\frac{t}{q_t} = \frac{1}{q_e} t + \frac{1}{k_2 q_e^2} \quad (4)$$

$$q_t = k_i t^{1/2} + C \quad (5)$$

Where:

q_e - the adsorption capacities under adsorption equilibrium,(mg/g);

q_t - the adsorption capacities at time t,(mg/g);

k_1 - the rate constant of the pseudo-first order kinetic model,(min^{-1});

k_2 - the rate constant of the pseudo-second order kinetic model, ($g^{-1}\cdot min^{-1}$);

k_i - intraparticle diffusion constant,[$mg/(g\cdot min^{1/2})$];

C - a constant expressing the extent of dominance of intraparticle diffusion, (mg/g).

The fitting outcomes are presented in Figure 10 and Table 7. Notably, the model plot for pseudo-second-order kinetics closely aligns with the experimental data [Figure 10c], boasting a correlation coefficient (R^2) of 0.9998. The results showed that ARM adsorption for CIP was controlled by chemical adsorption and the reaction rate constant is dictated by the square of the number of unoccupied adsorption sites on the adsorbent surface(Hu et al., 2011). The pseudo-first order kinetic model displayed a deviation from the experimental points, yielding an R^2 value of 0.88301 and a maximum adsorption capacity of 4.17 mg/g.

 doi:10.20944/preprints202405.1520.v1

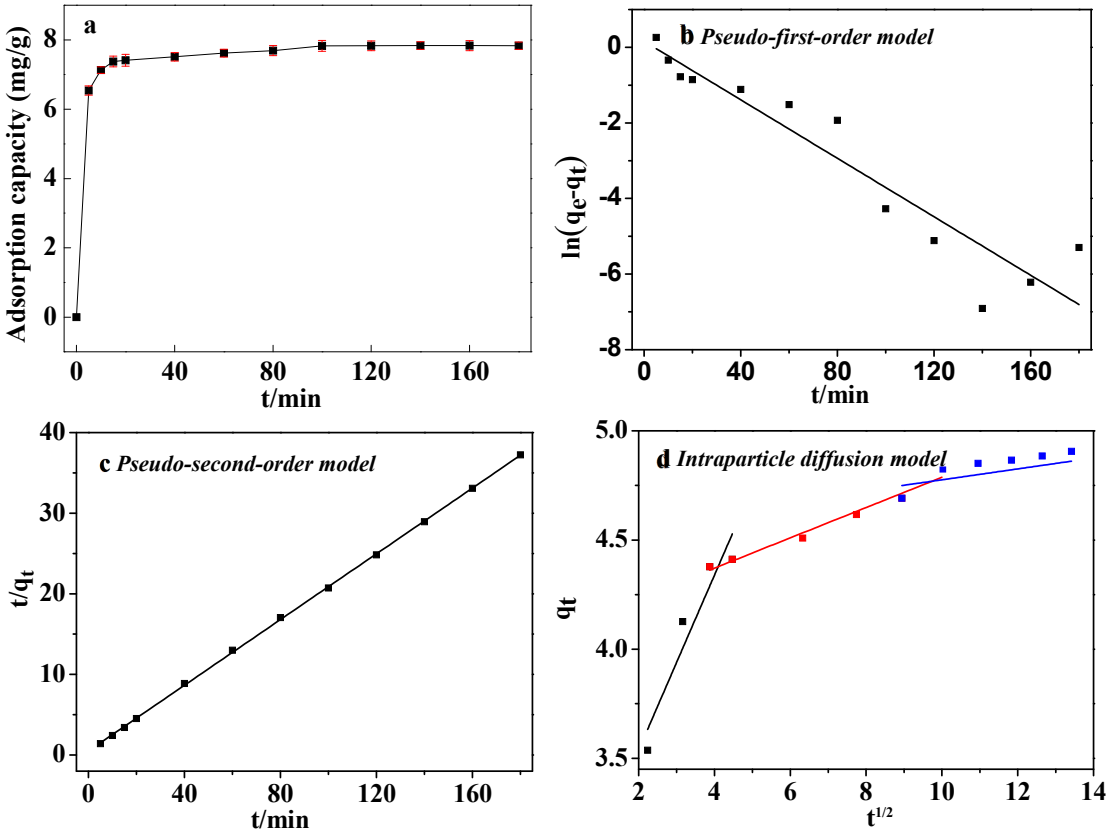

Figure 10. Fitting curves of different adsorption kinetics models (pH_0=3.04, T=45°C, [CIP]=30 mg/L) [ARM]=3.4 g/L, r=250 rpm).

Table 7. Constants of adsorption kinetics models.

Pseudo-first-order dynamic model	*Pseudo-second-order dynamic model*	*Intraparticle diffusion model*		
		The first phase	*The second phase*	*The third phase*
k_1=0.03869 (min^{-1})	k_2=0.023 [g/(mg·min)]	k_1=0.40054 (min^{-1})	k_2=0.06936 (min^{-1})	k_3=0.02236 (min^{-1})
q_e=4.17 (mg/g)	q_e=7.90 (mg/g)	C=6.74 (mg/g)	C=1.59 (mg/g)	C=1.03 (mg/g)
R^2=0.883	R^2=0.999	R^2=0.861	R^2=0.976	R^2=0.984

The intraparticle diffusion model [Figure 10d] showed that the whole adsorption process involved rapid adsorption, slow adsorption, and intraparticle diffusion. The fitting curve does not pass through the origin, which further implied that there existed other control processes (Ofomaja, 2008).

3.5. Adsorption Isotherm

Langmuir, Freundlich and Langmuir–Freundlich isotherm models were deployed to analyze the sorption behavior of CIP toward ARM. The Langmuir model (Eq.6) posits monolayer adsorption on homogeneous surfaces, while the Freundlich isotherm (Eq.7) characterizes multilayer adsorption on heterogeneous surfaces. The Langmuir– Freundlich model (Eq.8), amalgamating features from both Langmuir and Freundlich isotherms, incorporates three parameters into an empirical equation, rendering it more adept at delineating the extent of mono or multilayer adsorption within a system.

 doi:10.20944/preprints202405.1520.v1

$$\frac{C_e}{q_e} = \frac{C_e}{q_m} + \frac{1}{K_L q_m} \quad (6)$$

$$\ln q_e = \ln K_F + \frac{1}{n} \ln C_e \quad (7)$$

$$q_e = \frac{K_{LF} q_m C_e^{\,n}}{1 + K_{LF} C_e^{\,n}} \quad (8)$$

Where:

C_e - the solute equilibrium concentration, (mg/L);

q_e - equilibrium adsorption capacity, (mg/g);

q_m - theoretical maximum monolayer adsorption capacity, (mg/g);

K_L - the Langmuir adsorption constant related to adsorption energy, (L/mg);

K_F - the Freundlich constant related to removal efficiency of solute, (L/g);

n - constant characterising the adsorption strength;

K_{LF} - the Langmuir–Freundlich constant, (L/mg).

The isotherm fitting outcomes (Figure 11) alongside the error parameters and R^2 values (Table 8) indicated that all three isotherm models provided acceptable fits to the experimental data. Notably, the Freundlich and Langmuir–Freundlich models exhibited superior fit compared to the Langmuir model, suggesting that the adsorption process involved a combination of mono and multilayer adsorption. This implies that real adsorption took place on heterogeneous surfaces with varying adsorption sites, facilitated by multiple adsorption interactions. According to the Langmuir–Freundlich fitting results, the maximum adsorption capacity of CIP toward ARM increased with temperature, being 7.35 mg/g at 45°C, which conformed to the measured maximum adsorption capacity (7.84 mg/g).

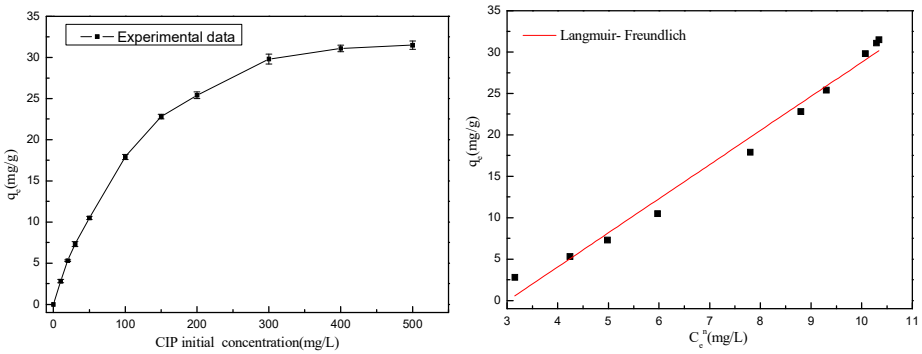

Figure 11. Fitting curves of Langmuir-Freundlich isotherm model (pH_0=3.04, T=45°C, [CIP]=10~500 mg/L, [ARM]=3.4 g/L, r=250 rpm).

Table 8. Parameters of adsorption isotherms for CIP adsorption onto ARM (ARM dosage: 3.4g/L; CIP initial concentration: 10~500 mg/L; initial solution pH: 3.0; adsorption temperature: 45°C).

Adsorption isotherm	Parameter 1	Parameter 2	Parameter 3	R^2
Langmuir	K_L=0.15 *(L/mg)*	q_{max}=5.63*(mg/g)*		0.992
Freundlich	K_F=276.95 *(L/g)*	n=1.47		0.993
Langmuir-Freundlich	K_{LF}=0.11 *(L/mg)*	q_{max}=7.35*(mg/g)*	n=0.51	0.983

Additionally, as depicted in Table 9, we conducted a comparative analysis of our adsorbents with those reported in the literature. Adsorbents with strong adsorption capacity generally come from the preparation of emerging materials. As a kind of solid waste, RM has the characteristics of cheap raw materials and simple modification, and the adsorption capacity of acidified red mud to

 doi:10.20944/preprints202405.1520.v1

CIP is higher than sodium alginate and kaolinite. These findings underscore the considerable potential of ARM as antibiotic adsorbents.

Table 9. Comparative assessment of CIP adsorption capacities across various adsorbents.

Adsorbents	*Adsorption capacity (mg/g)*	*pH*	*Temp(°C)*	*Ref.*
Magnetic N-doped porous carbon	1564	7.0	25	[Tang, et al.,2020]
Fe based MOF	868.6	6.8	15	[Jiang, et al.,2016]
Fe pillared clay	122.1	10	20	[Roca, et al.,2017]
Chitosan/Kaolin/Fe_3O_4	47.85	6.0	25	[Ma, et al.,2014]
Activated red mud	41.5	7.0	-	[Balarak et al., 2017]
Montmorillonite	23	-	-	[Chen et al., 2015]
Schorl	8.49	5.5	-	[Yin, et al.,2018]
Acidified red mud	7.84	3.0	45	This study
Kaolinite	6.31	3.5	25	[Li et al., 2011]
Sodium alginate hydrogel	2.90	2.0	25	[Yu et al., 2016]
Sodium alginate aerogel	2.87			
AC	1.86	-	25	[Avcı, et al.,2019]
ZnO nanoparticles	0.16	6.0	25	[Dhiman and Sharma,2019]

3.6. Adsorption Thermodynamics

Based on the Van't Hoff equation (Eq.9~10), ΔG^0, ΔH^0, and ΔS^0 can be calculated according to the adsorption constants of Langmuir isotherm at different temperatures:

$$\ln K_L = -\frac{\Delta H^0}{RT} + \frac{\Delta S^0}{R} \qquad (9)$$

$$\Delta G^0 = \Delta H^0 - T\Delta S^0 \qquad (10)$$

Where:

K_L - the Langmuir coefficient of adsorption equilibrium.

Figure 12 displayed a plot of ln K_L versus 1/T. From the slope and intercept of the straight line, ΔG^0, ΔH^0, and ΔS^0 were calculated, and the results are shown in Table 10. ΔG^0 is positive, indicating that the adsorption CIP toward ARM is a non-spontaneous process. ΔG^0 decreased from 2.06 to 0.87 kJ/mol with temperature increased from 25 to 55°C. That implied the adsorption performance of adsorbent strengthens with temperature (Reza et al., 2014). In addition, the positive ΔH^0 indicated that the adsorption process involves an endothermic reaction (Kumar, Rashid and Barakat, 2014).

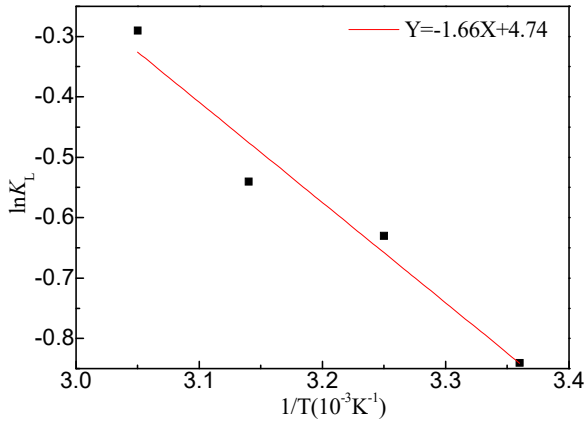

Figure 12. Van's Hoff linear graph (pH$_0$=3.04, T=25~55°C, [CIP]=30mg/L, [ARM]=3.4 g/L, r=250 rpm).

 doi:10.20944/preprints202405.1520.v1

Table 10. Thermodynamic parameter values for the adsorption.

Temperature(K)	*ΔH⁰(kJ/mol)*	*ΔS⁰(J/mol·k)*	*ΔG⁰(kJ/mol)*
298	13.80	39.41	2.06
308			1.66
318			1.27
328			0.87

3.7. ATR–FTIR Analysis of CIP and ARM

FTIR spectra of ARM before and after absorbing CIP are shown in Figure 13.

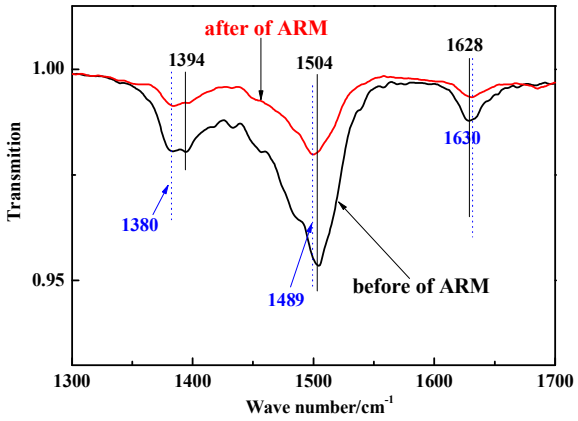

Figure 13. FTIR spectra of CIP and ARM before and after CIP adsorption(The black indicates acidified red mud (before adsorption); red indicates acidified red mud (after adsorption)).

In the case of ARM, the band observed at 1628 cm^{-1} originated from the stretching vibration of the Fe-O bond (hematite), while the bands at 1394 and 1504 cm^{-1} were attributed to the stretching vibration of the Al-O bond (boehmite) and the bending vibration of the O-H bond, respectively. These findings suggest the presence of adsorbed water within ARM. (Deihimi, Irannajad and Rezai, 2018).

After adsorbing CIP, the characteristic bands of the Al-O bond shifted from 1394 cm^{-1} to 1380 cm^{-1}, which was attributed to a complex reaction between Al-O in ARM and the -COO in CIP (Venkatesan and Narayanan, 2018). The O-H bonds at 1504 cm^{-1} shifted, implying that the adsorbed water in ARM was consumed (Castaldia, et al., 2010). The Fe-O bond at 1628 cm^{-1} shifted (albeit to no significant extent), showing that the C=O bond in CIP undergo a slight electrostatic interaction with Fe-O bond in ARM or be bound to the internal spherical surface of the ARM (Paras and Dharni, 2007).

3.8. Adsorption Stability of ARM

In order to investigate the stability of ARM for CIP adsorption, water with different uses and different pH was selected as the leaching solution to wash the adsorbed ARM. The experiment is shown in Figure 14.

 doi:10.20944/preprints202405.1520.v1

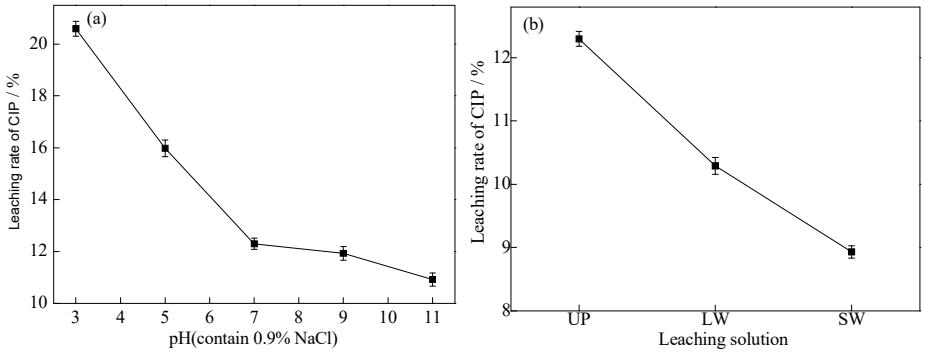

Figure 14. The efficiency of CIP leaching from different leaching solutions (pH_0=3.04, T=45°C, [CIP]=10~500 mg/L, [ARM]=3.4 g/L, r=250 rpm).

As shown in Figure 14a, the leaching rate of CIP decreases with increasing pH. When pH increases from 3 to 11, the corresponding leaching rate decreases from 20.59% to 10.92%. Compared with alkaline environments (pH=7-11), ARM with saturated adsorption exhibits poorer adsorption stability in acidic environments (pH=3-5). This is because at pH=3-5, H+competes with H4CIP3+, leading to an increase in the concentration of H4CIP3+in the leachate and a decrease in the stability of ARM.

As shown in Figure 14b, with a pH≈7, using ultrapure water (UP), lake water (LW), and sewage water (SW) as leachate, the leaching rates of CIP are 12.30%, 10.29%, and 8.93%, respectively. The stability is as follows: SW>LW>UP. Therefore, ARM exhibits higher stability in sewage water and lake water.

4. Conclusions

RM was acidified, characterized and used as absorbent for removing CIP. Based on the response surface optimisation model, the adsorption process was simulated, and the optimal conditions were obtained. The adsorption of CIP onto ARM adhered to a pseudo-second-order reaction (R^2=0.999). Additionally, the adsorption isotherm fitting indicated conformity to the Langmuir-Freundlich model (R^2= 0.983). Adsorption thermodynamics analysis showed that ARM adsorption for CIP was a non-spontaneous endothermic reaction. ATR–FTIR analysis suggested that there existed complex reaction between Al-O in ARM and the ester group –COO in CIP. And the C=O bond in CIP was likely to undergo a slight electrostatic interaction or be bound to the internal spherical surface of ARM. The results showed that ARM has potential application for CIP removal in water.

Acknowledgments: The authors gratefully acknowledge the financial support provided by the Shaanxi Natural Science Foundation of China (Grant No. 2023-JC-QN-0121) and the Key Laboratory Project of the Education Department of Shaanxi Province (Grant No. 21JS001) and Shaanxi University of Technology talent start-up project (Grant No. SLGRCQD2112).

References

1. Atasoy A., (2005), An investigation on characterization and thermal analysis of the aughinish red mud, *Journal of Thermal Analysis and Calorimetry*, 81,357-361.
2. Avcı A., Inci I., Baylan N., (2019), A comparative adsorption study with various adsorbents for the removal of Ciprofloxacin hydrochloride from water, *Water Air Soil Pollut*. 230 (10),250.
3. Balarak D., Joghataei A., Mostafapour F.K., Bazrafshan E., Pharm J., (2017), Ciprofloxacin antibiotics removal from effluent using heat-acid activated Red Mud, *Journal of Pharmaceutical Research International*,20(5),1-8.
4. Castaldia P., Silvetti M., Enzob S. Melis P., (2010), Study of sorption processes and FT-IR analysis of arsenate sorbed onto red muds(a bauxite ore processing waste), *Journal of Hazardous Materials*, 175,172–178.
5. Chen H., Gao B., Yang L. Y., Ma L. Q., (2015), Montmorillonite enhanced ciprofloxacin transport in saturated porous media with sorbed ciprofloxacin showing antibiotic activity, *Journal of Contaminant Hydrology*, 173, 1-7.

 doi:10.20944/preprints202405.1520.v1

6. Deihimi N., Irannajad M., Rezai B., (2018), Characterization studies of red mud modification processes as adsorbent for enhancing ferricyanide removal, *Journal of Environmental Management*, 206, 266-275.
7. Dhiman N., Sharma N., (2019), Batch adsorption studies on the removal of ciprofloxacin hydrochloride from aqueous solution using ZnO nanoparticles and groundnut (Arachis hypogaea) shell powder: a comparison,*Indian Chemical Engineer,* 61 (1), 67.
8. Fang H., Liang W., Ma C., et al.,(2023),Effect of interaction between Pd and Fe in modified red mud on catalytic decomposition of toluene, *Environmental Science Pollution Research*,1-16.
9. Gu H. N., Wang N., Liu S. R., (2012), Radiological restrictions of using red mud as building material additive, *Waste Management & Research*, 30(9), 961-965.
10. Guru, S., Amritphale, S. S., Mishra, J., Joshi S., (2019), Multicomponent red mud-polyester composites for neutron shielding Application, *Materials Chemistry and Physics*, 224,369-375.
11. Hu X. J., Wang J. S., Liu Y. G., Li X., Zeng G. M., Bao Z. L., Zeng X. X., Chen A. W., Long F., (2011), Adsorption of chromium (VI) by ethylenediamine-modified cross-linked magnetic chitosan resin: isotherms, kinetics and thermodynamics, *Journal of Hazardous Materials*, 185(1), 306-314.
12. Hua Y. M., Heal K. V., Friesl-Hanl W., (2017), The use of red mud as an immobiliser for metal/metalloid-contaminated soil: A review, *Journal Hazard Mater*, 325, 17-30.
13. Huang W. W., Wang S.B., Zhu Z. H., Li L., Yao X. D., Rudolph V., Haghseresht F., (2008), Phosphate removal from wastewater using red mud, *Journal Hazardous Material*, 158, 35-42.
14. Jayasankar K., Ray P. K., Chaubey A. K., Padhi A., Satapathy B.K., Mukherjee P.S., (2012), Production of pig iron from red mud waste fines using thermal plasma technology, *International Journal of Minerals, Metallurgy and Materials*, 19(8),679-684.
15. Jiang C., Zhang X., Xu X., Wang L., (2016), Magnetic mesoporous carbon material with strong ciprofloxacin adsorption removal property fabricated through the calcination of mixed valence Fe based metal-organic framework, Journal of Porous Materials, 23 (5),1297.
16. Jollet V., Gissane C., Schlaf M., (2014), Optimization of the neutralization of red mud by pyrolysis bio-oil using a design of experiments approach, *energy & environmental science*, 3, 1125-1133.
17. Kolpin D. W., Furlong E. T., Meyer M., (2002) Pharmaceuticals, hormones, and other organic wastewater contami- nants in U.S.streams, 1999-2000: A national reconnaissance, *Environmental Science & Technology*,36, 1202-1211.
18. Kumar R., Rashid J., Barakat M. A., (2014), Synthesis and characterization of a starch-AlOOH-FeS_2 nanocomposite for the adsorption of congo red dye from aqueous solution, *RSC Advances*, 4, 38334-38340.
19. Liang W., Zhu Y., Ren S., Li Q., Song L., Shi X., (2021), Catalytic combustion of chlorobenzene at low temperature over Ru-Ce/TiO2: high activity and high selectivity, *Applied Catalysis A: General*,623,118257.
20. Liang W. J., Tao Q. Y., Fang H. P., Zhang C. H., Liu J., Bin F., Kang R. N., (2024),Modification of red mud catalyst using oxalic acid-assisted UV treatment for toluene removal,*Catalysis Today*, 433,114675.
21. Li C. M., Yu J., Li W. S., He Y., Qiu Y. L., Li P., Wang C., Huang F. L., Wang D. L., Gao S. Q., (2018), Immobilization, enrichment and recycling of Cr(VI) from wastewater using a red mud/carbon material to produce the valuable chromite ($FeCr_2O_4$), *Chemical Engineering Journal*, 350, 1103-1113.
22. Li Z. H., Hong H. L., Liao L.B., Ackley C. J., Schulz L. A., MacDonald R. A., Mihelich A. L., Emard S. M., (2011), A mechanistic study of ciprofloxacin removal by kaolinite, *Colloids and Surfaces B: Biointerfaces*, 88, 339-344.
23. Liu Y., Lin C., Wu Y., (2007), Characterization of red mud derived from a combined Bayer process and bauxite calcination method, Journal of Hazardous Materials, 146, 255-261.
24. Ma W., Dai J., Dai X., Yan Y., (2014), Preparation and characterization of Chitosan/Kaolin/Fe_3O_4 magnetic microspheres and their application for the removal of Ciprofloxacin, *Adsorption Science & Technology*, 32 (10), 775.
25. Martins A. F., Vasconcelos T. G., Henriques D. M., Frank C. S., (2008), Concentration of ciprofloxacin in Brazilian hospital effluent and preliminary risk assessment: a case study, *Clean-Soil Air Water*, 36, 264-269.
26. Manoj K. S., Sandip M., Saswati S. D.,Pranati B., Raj K. P., (2013), Removal of Pb(II) from aqueous solution by acid activated red mud, *Journal of Environmental Chemical Engineering*, 1,1315-1324.
27. Ni F., He J. S., Wang Y. B., Luan Z. K., (2015), Preparation and characterization of a cost-effective red mud/ polyaluminum chloride composite coagulant for enhanced phosphate removal from aqueous solutions, *Journal of Water Process Engineering*, 6, 158-165.
28. Ofomaja A. E., (2008), Kinetic study and sorption mechanism of methylene blue and methyl violet onto mansonia (mansonia altissima) wood sawdust, *Chemical Engineering Journal*, 143(1-3), 85-95.
29. Orimolade B. O., Oladipo A. O., Idris A. O.et al.,(2023),Advancements in electrochemical technologies for the removal offluoroquinolone antibiotics in wastewater: A review, *Science of the Total Environment*,881,163522.
30. Paras T., Dharni V., (2007), Spectroscopic investigation of ciprofloxacin speciation at the goethite-water interface, *Environmental Science & Technology*, 41(9), 3153-3158.

 doi:10.20944/preprints202405.1520.v1

31. Rakshit S., Sarkar D., Elzinga E. J., Punamiya P., Datta R., (2013), Mechanisms of ciprofloxacin removal by nano-sized magnetite, *Journal of Hazardous Materials*, 246-247, 221-226.
32. Ren J., Chen J., Guo W., Yang B., Qin X. P., Du P., (2019), Physical, chemical, and surface charge properties of bauxite residue derived from a combined process, *Journal of Central South University*, 26(2), 373-382.
33. Ren J., Chen J., Han L., Wang M., Yang B., Du P., Li F. S., (2018), Spatial distribution of heavy metals, salinity and alkalinity in soils around bauxite residue disposal area, *Science of the Total Environment*, 628-629, 1200-1208.
34. Reza R. A., Ahmaruzzaman M., Sil, A. K., Gupta V. K., (2014), Comparative adsorption behavior of ibuprofen and clofibric acid onto microwave assisted activated bamboo waste, *Industrial and Engineering Chemistry Research*, 53, 9331-9339.
35. Roca Jalil M.E., Baschini M., Sapag K., (2017), Removal of Ciprofloxacin from aqueous solutions using pillared clays,Materials, 10 (12), 1345.
36. Saha S., Sarkar P., (2012), Arsenic remediation from drinking water by synthesized nano-alumina dispersed in chitosan-grafted polyacry- lamide, *Journal of Hazardous Materials*, 227-228, 68-78.
37. Schmalenberger A., O'sullivan O., Gahan J., Cotter P. D., Courtney R., (2013), Bacterial communities established in bauxite residues with different restoration histories, *Environmental Science & Technology*, 47(13), 7110-7119.
38. Tang Y., Chen Q., Li W., Xie X., Zhang W., Zhang X., Chai H., Huang Y.,(2020), Engineering magnetic N-doped porous carbon with super-high ciprofloxacin adsorption capacity and wide pH adaptability, *Journal of Hazardous Materials,* 388,122059.
39. Venkatesan G., Narayanan S. L., (2018), Synthesis of Fe_2O_3-coated and HCl-treated bauxite ore waste for the adsorption of arsenic (III) from aqueous solution: isotherm and kinetic models, *Chemical Engineering Communications*, 205(1), 34-46.
40. Walsh C., (2003), *Antibiotics: Actions, Origins, Resistance*, ASM Press, Washington, D. C.
41. Wang Y., Yu Y. G., Li H. Y., Shen C. C., (2016), Comparison study of phosphorus adsorption on different waste solids: Fly ash, red mud and ferric-alum water treatment residues, *Journal of Environmental Science (China)*, 50, 79-86.
42. Wang Y. Z., Zhang L. Y., Yan Z. W., Shao L. H., Kang H., Wei G. T., (2015), Application of a low-cost bagasse carbon-red mud (BCRM) adsorbent for adsorption of methylene blue cationic dye: adsorption performance, kinetics, isotherm, and thermodynamics, *Desalination and Water Treatment*, 57(15),1-11.
43. Wu J., Gong Z., Lu C., et al.(2018). Preparation and performance ofmodified red mud-based catalysts for selective catalytic reductionof NOx with NH_3. *Catalysts*, 8(1): 35.
44. Xue S. G., Zhu F., Kong X. F., Wu C., Huang L., Huang N., Hartley W., (2016), A review of the characterization and revegetation of bauxite residues (Red mud), *Environmental Science and Pollution Research*, 23(2), 1120-1132.
45. Yan X. M., Miao P., Chang G. Z., Guo Q. J., (2018), Characteristics of microstructures and reactivities during steam gasification of coal char catalyzed by red mud, *Chemical Industry and Engineering Progress*, 37(5), 1753-1759.
46. Ye J., Cong X. N., Zhang P. Y., Hoffmann E., Zeng G. M., Liu Y., Fang W., Wu Y., Zhang H. B., (2015), Interaction between phosphate and acid-activated neutralized red mud during adsorption process, *Applied Surface Science*, 356: 128-134.
47. Yin D., Xu Z., Shi J., Shen L., He Z., (2018), Adsorption characteristics of ciprofloxacin on the schorl: kinetics, thermodynamics, effect of metal ion and mechanisms, *Journal of Water Reuse and Desalination*,8 (3),350.
48. Yu F., Li Y., Han S., Ma J., (2016), Adsorptive removal of ciprofloxacin by sodium alginate/graphene oxide composite beads from aqueous solution, *Journal of Colloid and Interface Science*, 484, 196-204.
49. Zhang J., Hayat K., Zhang X. M., Tong J.M., Xia S. Q., (2010), Separation and purification of flavonoid from ginkgo extract by polyamide resin, *Separation Science and Technology*,45(16),2413-2419.
50. Zhilkina A. V., Gordienko A. A., Prokudina N. A., Trusov L. I., Kuz'micheva G. M., Dulina N. A., Savinkina E. V., (2013), Determination of the size of particles of highly dispersed materials by low temperature nitrogen adsorption, *Russian Journal of Physical Chemistry A*, 87,674-679.
51. Zhu X. B., Li W., Tang S. Zeng M. J., Bai P. Y., Chen L. J., (2017), Selective recovery of vanadium and scandium by ion exchange with D201 and solvent extraction using P507 from hydrochloric acid leaching solution of red mud, *Chemosphere*, 175, 365-372.